Chinese Chemical Letters 33 (2022) 4367–4374

Contents lists available at ScienceDirect

Chinese Chemical Letters

journal homepage: www.elsevier.com/locate/cclet

Flower-like $NiCo_2S_4$/NiFeP/NF composite material as an effective electrocatalyst with high overall water splitting performance

Jing Jiang[a,b], Fengyan Li[a,b], Hui Su[a,b], Yangqin Gao[a,b], Ning Li[a,b], Lei Ge[a,b,*]

[a] State Key Laboratory of Heavy Oil Processing, College of New Energy and Materials, China University of Petroleum Beijing, Beijing 102249, China
[b] Department of Materials Science and Engineering, College of New Energy and Materials, China University of Petroleum Beijing, Beijing 102249, China

ARTICLE INFO

Article history:
Received 23 August 2021
Revised 8 November 2021
Accepted 13 December 2021
Available online 17 December 2021

Keywords:
$NiCo_2S_4$
Electrocatalyst
NiFeP
Hydrogen evolution reaction
Water splitting

ABSTRACT

Rational design and building of high efficiency, secure and inexpensive electrocatalyst is a pressing demand and performance to promote sustainable improvement of hydrogen energy. The bifunctional electrocatalysts for oxygen evolution reaction (OER) and hydrogen evolution response (HER) with high catalytic performance and steadiness in the equal electrolyte are extra treasured and meaningful. Herein, a unique three-dimensional (3D) structure electrocatalyst for $NiCo_2S_4$ growing on the flower-like NiFeP was designed and synthesized in this study. The results show that the flower-like $NiCo_2S_4$/NiFeP/NF composite electrocatalyst has large specific surface area, appropriate electrical conductivity, and greater lively websites uncovered in the three-dimensional structure, and affords extraordinary electrocatalytic overall performance for the ordinary water splitting. In alkaline solution, the OER and HER overpotentials of $NiCo_2S_4$/NiFeP/NF only need 293 mV and 205 mV overpotential to provide the current densities of 100 mA/cm^2 and 50 mA/cm^2, respectively. This high electrocatalytic activity exceeds the catalytic activity of most nickel-iron based electrocatalysts for OER and HER process. Accordingly, the optimized $NiCo_2S_4$/NiFeP/NF sample has higher stability (24 h) at 1.560 and 10 mA/cm^2, which extensively speeds up the overall water splitting process. In view of the above performance, this work offers a fine approach for the further improvement of low fee and excessive effectivity electrocatalyst.

In recent years, with the contradiction between global energy demand and resource, and environment constraints becoming increasingly prominent [1], we urgently need to find a green and efficient alternative energy. Compared with other green energy, hydrogen energy is a new type of energy with the most development potential [2], due to the fact of its wealthy resources, high energy density, free from geographical and environmental conditions. Among them, compared with chlor-alkali industrial [3], chemical raw materials [4–6] (methanol cracking, ethanol pyrolysis, liquid ammonia cracking, *etc.*), petrochemical resources [7,8] (oil cracking, water gas preparation method, *etc.*) and new preparation method to produce hydrogen [9–11] (biomass, photochemical, *etc.*), electrochemical water splitting will become the main technology of hydrogen production [12,13] due to the high purity, clean green with the development of new type catalysts.

At present, precious metal-based materials with high catalytic activity have limited large-scale applications due to high prices and relatively small reserves in nature [14]. A large number of studies have showed that electrocatalysts containing nickel, iron, and cobalt are relatively inexpensive and have higher electrocatalytic activity [15–18]. Recently, transition metallic phosphides [19,20] and transition metallic sulfides [21] have additionally been significantly explored as candidate substances for non-noble metal-based electrocatalysts for electrolysis of water. According to reports, transition metal phosphides will increase the charge transfer rate and change the electronic structure to optimize the sorption energy, however its inherent low conductivity and insufficient active centers severely limit the improvement of their catalytic performance for water splitting [19,22]. Similarly, the ternary nickel-cobalt sulfide exhibits a synergistic effect between different components and has high oxygen evolution electrocatalytic activity, however the stability is still unsatisfactory [21,23–25]. In addition, compared with single-component materials, the interaction between the two components of the composite structure shows excellent electrocatalytic performance and has become a research hotspot [26,27]. Therefore, it is very necessary to accurately design and finely synthesize high-efficiency, durable, and low-cost dual-functional electrocatalysts.

* Corresponding author at: State Key Laboratory of Heavy Oil Processing, College of New Energy and Materials, China University of Petroleum Beijing, Beijing 102249, China.
E-mail address: gelei@cup.edu.cn (L. Ge).

https://doi.org/10.1016/j.cclet.2021.12.028
1001-8417/

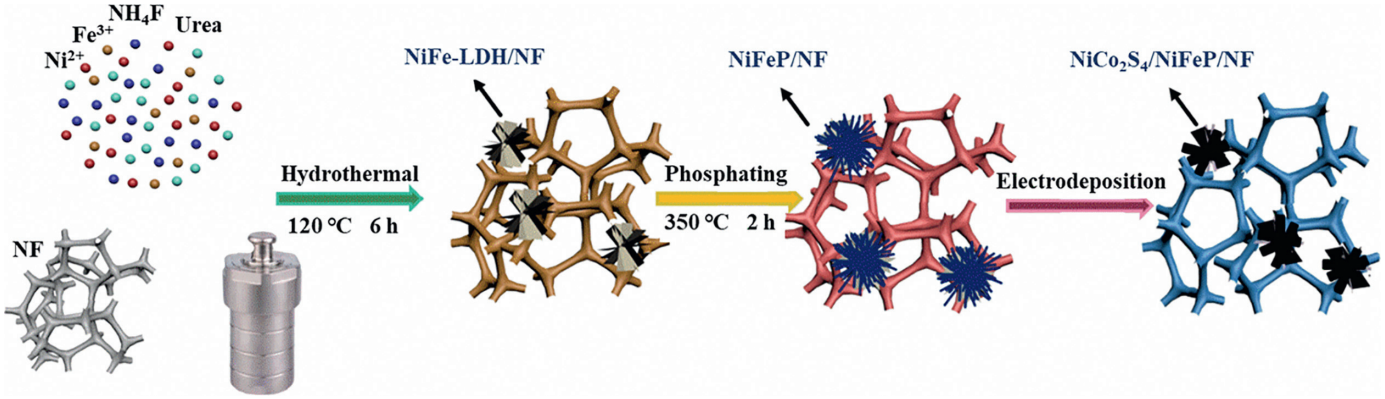

Scheme 1. Schematic diagram of $NiCo_2S_4$/NiFeP/NF synthesis process on nickel foam.

Herein, stimulated by using the above ideas, we have assembled a three-dimensional flower-shaped $NiCo_2S_4$/NiFeP/NF electrocatalyst through an easy one-step hydrothermal method, phosphating, and electrodeposition technological to gain a surprisingly environmentally friendly and steady dual-function electrolysis for water splitting. $NiCo_2S_4$/NF, NiFe-LDH/NF and NiFeP/NF were synthesized as comparison samples, and the effect of three-dimensional flowered $NiCo_2S_4$/NiFeP/NF composites on the catalytic activity was investigated and confirmed. As expected, the organized three-dimensional flower-like $NiCo_2S_4$/NiFeP/NF composite confirmed properly catalytic overall performance for both HER and OER in 1 mol/L KOH. The overpotential of HER at 50 mA/cm^2 was 205 mV, and that of OER at 100 mA/cm^2 was 293 mV. In addition, the three-dimensional flower-shaped $NiCo_2S_4$/NiFeP/NF showed 10 mA/cm^2 in a two-electrode system at 1.560 V to achieve high-efficiency overall water splitting activity, and exhibited remarkable durability for 24 h, which was a promising high-performance dual-function electrocatalyst.

Scheme 1 shows the synthesis process of $NiCo_2S_4$/NiFeP/NF on a nickel foam substrate. Under the action of using urea as a chelating agent and ammonium fluoride as a structure directing agent, the OH^- released in urea reacts with the added Fe^{3+} and Ni^{2+} ions to form NiFe-LDH through a simple hydrothermal reaction. Specifically, ammonium fluoride (NH_4F) assists the morphology evolution of NiFe-LDH nanomaterials [28]. Using the as-synthesized NiFe-LDH as the precursor, $NiCo_2S_4$/NiFeP/NF electrocatalyst was prepared by 350 °C high temperature phosphating and electrodeposition process.

The X-ray diffraction pattern of $NiCo_2S_4$/NiFeP/NF (Ni:Co = 1:1) is illustrated in Fig. 1. Since the diffraction peak intensity of the foamed nickel substrate is too powerful, it has masked the diffraction peaks of the electrocatalyst, so the electrocatalyst sample has been scraped off the foamed nickel substrate for XRD measurement (Fig. S1 in Supporting information). Among them, the 19.8° diffraction peak may be caused by the low purity of the sample scraped from the foamed nickel. As shown in Fig. 1, all diffraction peaks in $NiCo_2S_4$/NiFeP/NF composite correspond to $NiCo_2S_4$ (JCPDS No. 200782), Ni_2P (JCPDS No. 741385) and FeP (JCPDS No. 781443). $NiCo_2S_4$/NiFeP/NF sample has three sharp diffraction peaks at 31.58°, 50.46°, 55.33°, corresponding to the (311), (511), (400) crystal planes of $NiCo_2S_4$, respectively. The peaks at 47.36° and 54.19° are attributed to the (210) and (300) crystal planes of Ni_2P, and the peaks at 46.29° and 48.31° are attributed to the (112) and (211) crystal planes of FeP. Therefore, it can be speculated that $NiCo_2S_4$/NiFeP/NF have successfully prepared.

The surface morphologies of NF, NiFe-LDH/NF, $NiCo_2S_4$/NF, NiFeP/NF, $NiCo_2S_4$/NiFeP/NF were characterized by the scanning

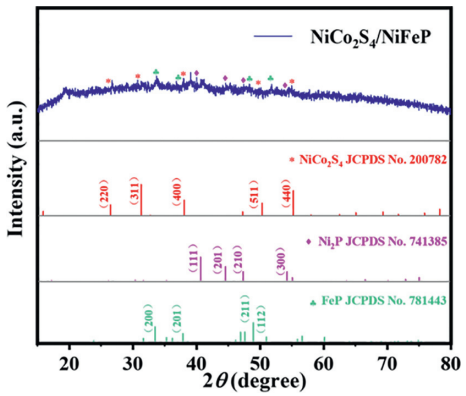

Fig. 1. XRD patterns of $NiCo_2S_4$/NiFeP powder peeled off on nickel foam.

electron microscope (SEM). In Fig. S2a (Supporting information), it can be seen that the surface of NF is smooth and clean. According to the SEM image of $NiCo_2S_4$/NF (Figs. S2b and c in Supporting information), it can be seen that a good deal of $NiCo_2S_4$ nanosheets with a thickness of several nanometers are deposited on the surface of NF, and they are connected with each other, which is conducive to promoting the diffusion of electrolyte ions. Figs. S2d and e (Supporting information) show the NiFe-LDH/NF nanosheets with a thickness of a few nanometers and a diameter of 200–500 nm grown under the guidance of the ammonium fluoride structure. The flower-like nanostructures assembled in sheet form and the ultra-thin nanosheets provide the possibility for the electrolyte to fully contact the active center. Compared with NiFe-LDH/NF, the size of NiFeP/NF catalyst does not change under high temperature phosphating at 350 °C, and the nano flakes are slightly damaged, however the nano-curd structure is basically maintained, as shown in Figs. S2f and g (Supporting information). In Fig. 2a and Fig. S2h (Supporting information) $NiCo_2S_4$/NiFeP/NF, the thickness of the nanosheets increases, which may be caused by the sedimentation of smaller $NiCo_2S_4$ nanosheets surfacewise of the large NiFeP nanosheets. The multi-level structure is conducive to the formation of more abundant space, further increasing the exposure of active sites, thereby obtaining more excellent electrocatalytic performance [29]. The element mapping of the $NiCo_2S_4$/NiFeP/NF sample is presented in Figs. 2b–i. It can be seen that the Ni, Fe, Co, P and S elements are even-distributed on the surface of the sample, so the EDS results are in accordance with the XRD results. NiFe-LDH/NF is assembled from a large number of nanosheets, and the lattice fringe of 0.26 nm matches the (012) crystal plane of NiFe-LDH, as

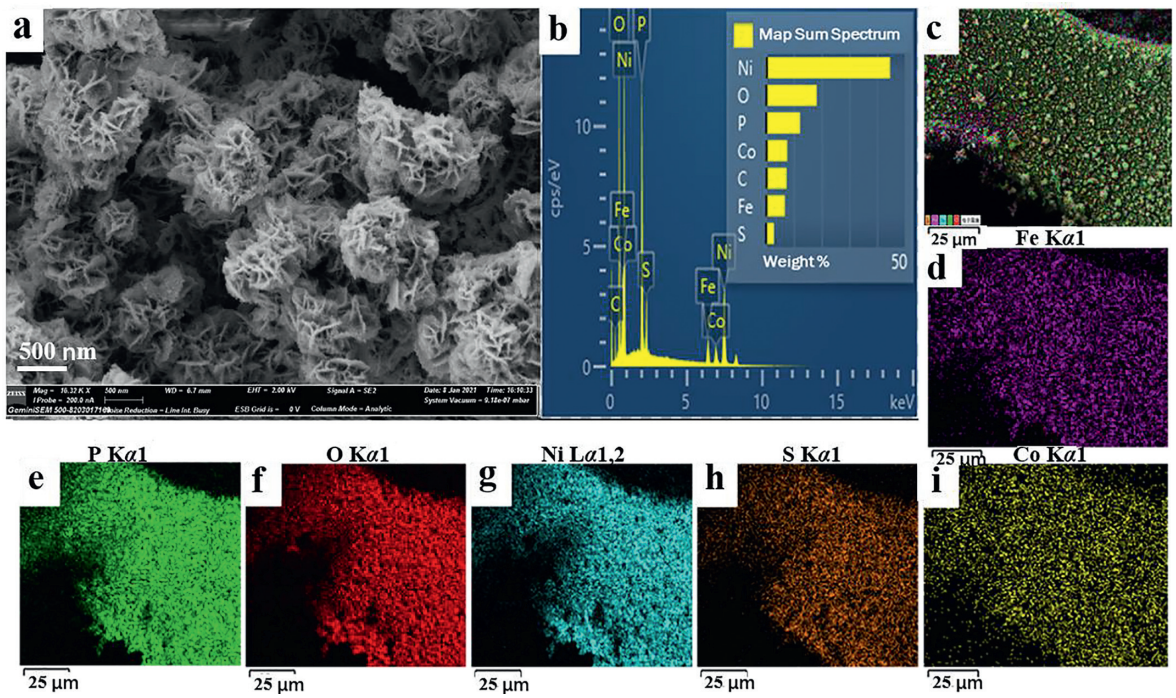

Fig. 2. (a, b) SEM images and EDS (c–i) images of $NiCo_2S_4$/NiFeP/NF sample.

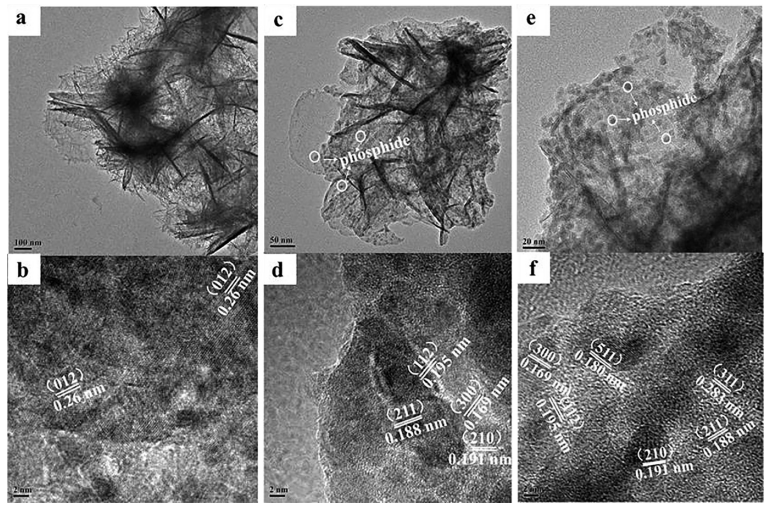

Fig. 3. (a, b) The TEM and HRTEM images of NiFe-LDH/NF (c, d) NiFeP/NF (e, f) $NiCo_2S_4$/NiFeP/NF.

shown in Fig. 3b. Transmission electron microscopy (TEM) results show that NiFeP/NF sample presents a porous nano-sheet structure, which is conducive to electrolyte penetration and contact.

The microstructures of NiFe-LDH/NF, NiFeP/NF and $NiCo_2S_4$/NiFeP/NF samples were further explored by transmission electron microscopy (TEM). The sample was separated from the NF by an ultrasonic apparatus. Figs. 3a, c and e further confirms the ultrathin nano-spherical structure of the electrocatalyst. In Fig. 3b, the lattice fringes at 0.26 nm can be attributed to the (012) crystal plane of NiFe-LDH. As shown in Fig. 3c, after high-temperature phosphating, phosphide clusters appear on the ultra-thin nanospheres. In Fig. 3d, the lattice fringes at 0.191 nm and 0.169 nm can be attributed to the (210) and (300) crystal planes of Ni_2P, and the lattice fringes at 0.195 nm and 0.188 nm act in response to the (112) and (211) crystal planes of FeP, respectively. Typically, as shown in HRTEM, $NiCo_2S_4$/NiFeP/NF not only shows the lattice fringes of Ni_2P and FeP, but also confirms the existence of $NiCo_2S_4$ phase. As shown in Fig. 3f, the 0.283 nm and 0.180 nm lattice fringes match the (311) and (511) crystal planes of $NiCo_2S_4$. TEM and HRTEM results indicate the successful preparation of $NiCo_2S_4$/NiFeP/NF composite sample.

The surface chemical composition and state of $NiCo_2S_4$/NiFeP/NF were characterized by XPS technique. Fig. 4a confirms the presence of Ni, Co, Fe, P and S elements, which is consistent with EDS results. For the high-resolution X-ray photoelectron spectroscopy of Ni 2p (Fig. 4b), the two characteristic peaks with binding energies of 855.9 eV and 873.5 eV are attributed to Ni $2p_{3/2}$ and Ni $2p_{1/2}$ orbitals, respectively. The two peaks at 861.7 eV and 879.9 eV are attributed to the satellite peaks of Ni $2p_{3/2}$ and Ni $2p_{1/2}$, respectively. It is well worth noting

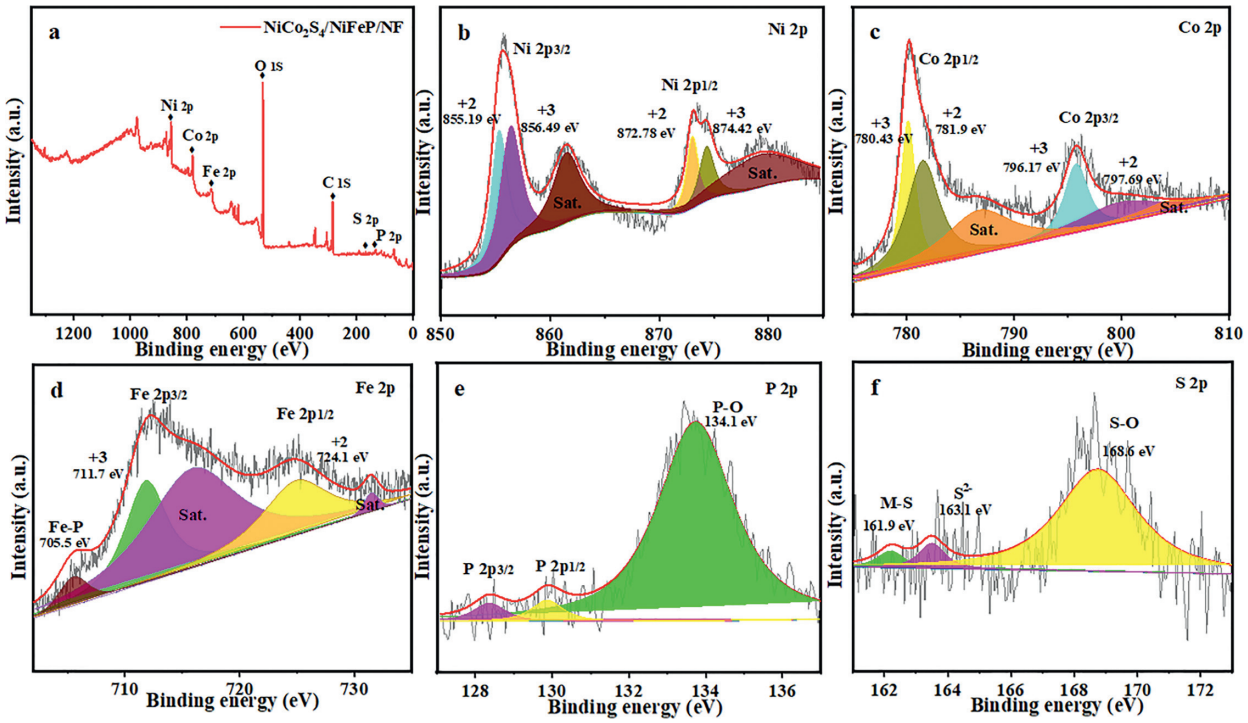

Fig. 4. (a) XPS measurement spectrum and high-resolution XPS spectrum of $NiCo_2S_4$/NiFeP/NF in (b) Ni 2p, (c) Co 2p, (d) Fe 2p, (e) P 2p, (f) S 2p region.

that the peaks at 855.19 eV and 872.78 eV are attributed to Ni^{2+} species, and the peaks at 856.49 eV and 874.42 eV are attributed to Ni^{3+}, which confirms that the valence states of Ni in $NiCo_2S_4$ /NiFeP/NF are both +2 and +3 [30]. As shown in Fig. 4c, Co^{2+} (781.9 eV, 797.69 eV) and Co^{3+} (780.43 eV, 796.17 eV) species can also be identified [31]. Among them, it has been confirmed that the Ni and Co peaks shift relative to a single sample when $NiCo_2S_4$ and NiFeP form the composite material, indicating that a strong chemical bond is formed between $NiCo_2S_4$ and NiFeP [32]. The high-resolution Fe 2p-XPS spectrum (Fig. 4d) presents that the Fe element exhibits the coexistence of +2 valence (724.1 eV) and +3 valence (711.7 eV). Among them, the peaks with binding energies of 716.6 eV and 731.0 eV are satellite peaks, and the peaks at 705.5 eV are related to Fe-P species, which is consistent with previous work [32–34]. Fig. 4e shows that the XPS peaks with binding energies of 128.6 eV and 129.5 eV belong to P $2p_{3/2}$ and P $2p_{1/2}$ orbitals. The peak corresponding to P-O bond (134.1 eV) is formed due to the oxidation of NiCo2S4/NiFeP/NF in air [35]. Correspondingly, S 2p can be divided into three peaks of 161.9 eV (metal-sulfur bond), 163.1 eV (low coordination sulfite ion), and 168.6 eV (S-O bond) [36,37], which is consistent with previous reports (Fig. 4f). XPS analysis results indicate that $NiCo_2S_4$/NiFeP/NF has the +2, +3 valence of Ni, Fe, Co and the mixed valence of S^{2-}.

Using a traditional three-electrode system, the HER performance of $NiCo_2S_4$/NiFeP/NF sample was investigated in 1 mol/L KOH electrolyte. First of all, the HER performance of the electrocatalyst is affected by synthesis temperature. In this experiment, NiFe-LDH/NF was phosphated at 300, 350 and 400 °C heating rate of 2 °C/min, and the optimal phosphating temperature of the precursor NiFeP/NF (Fig. S3 in Supporting information) was determined to be 350 °C. Too low phosphating temperature is not conducive to the formation of Ni_2P and FeP, and too high phosphating temperature will destroy the original structure of the catalyst [38]. In addition, the Ni/Co ratio of the electrodeposited $NiCo_2S_4$ and the electrodeposited ring layer also affect the activity of the $NiCo_2S_4$/NiFeP/NF electrocatalyst. As shown in Fig. S4a (Supporting information), according to the linear sweep voltammetry (LSV) curves of hydrogen evolution with different Ni/Co ratios, the ratios of Ni:Co are 0:5, 1:4, 2:3, 3:2, 4:1, 5:0. When Ni:Co = 1:1, $NiCo_2S_4$/NiFeP/NF shows the best hydrogen evolution activity. Fig. S4b (Supporting information) presents that the HER activity of $NiCo_2S_4$ electrodeposited 4 turns on NiFeP/NF is the best. For comparison, the HER performance of $NiCo_2S_4$/NF, NiFe-LDH/NF, and NiFeP/NF were also tested. As expected, the $NiCo_2S_4$/NiFeP/NF electrocatalyst performed the best HER activity (Fig. 5a), which can be attributed to the synergy and interaction between $NiCo_2S_4$ and NiFeP species. $NiCo_2S_4$/NiFeP/NF reaches current density of 50 mA/cm^2 with an overpotential of 205 mV, which is decrease than pure $NiCo_2S_4$/NF (295 mV) and NiFeP/NF (225 mV) electrocatalysts.

To further investigate the catalytic mechanism, the linear part of the polarization curve was fitted, and the calculated Tafel slope was used to estimate the catalytic kinetics. According to Tafel equation: $\eta = b\log j + a$, where η is the overpotential, j is the current density, and b is the Tafel slope. The Tafel slope of $NiCo_2S_4$/NiFeP/NF is 99 mV/dec, which is much lower than $NiCo_2S_4$/NF (156 mV/dec), NiFe-LDH/NF (123 mV/dec), NiFeP/NF (114 mV/dec), indicating good electron transport and reaction kinetics, As shown in Fig. 5b. In addition, the best HER activity of $NiCo_2S_4$/NiFeP/NF is related to its high electrochemically active specific surface area (Fig. 5c, Fig. S6 in Supporting information), which is mainly due to the increase in the quantity of active sites in the composite structure [39]. For HER, the double-layer capacitance (Cdl) value of $NiCo_2S_4$/NiFeP/NF is determined to be 31.27 mF/cm^2, which is significantly greater than $NiCo_2S_4$/NF (2.84 mF/cm^2), NiFe-LDH/NF (6.4 mF/cm^2) and NiFeP/NF (14.08 mF/cm^2). In order to explore the charge transfer capability, electrochemical impedance spectroscopy (EIS) is evaluated in a 1 mol/L KOH aqueous solution. As shown in Fig. 5d, the charge transfer resistance ranges from $NiCo_2S_4$/NF (R_{ct} = 153.03 Ω), NiFeP/NF (R_{ct} = 40.27 Ω) to $NiCo_2S_4$/NiFeP/NF (R_{ct} = 9.23 Ω), indicating that the composite structure can

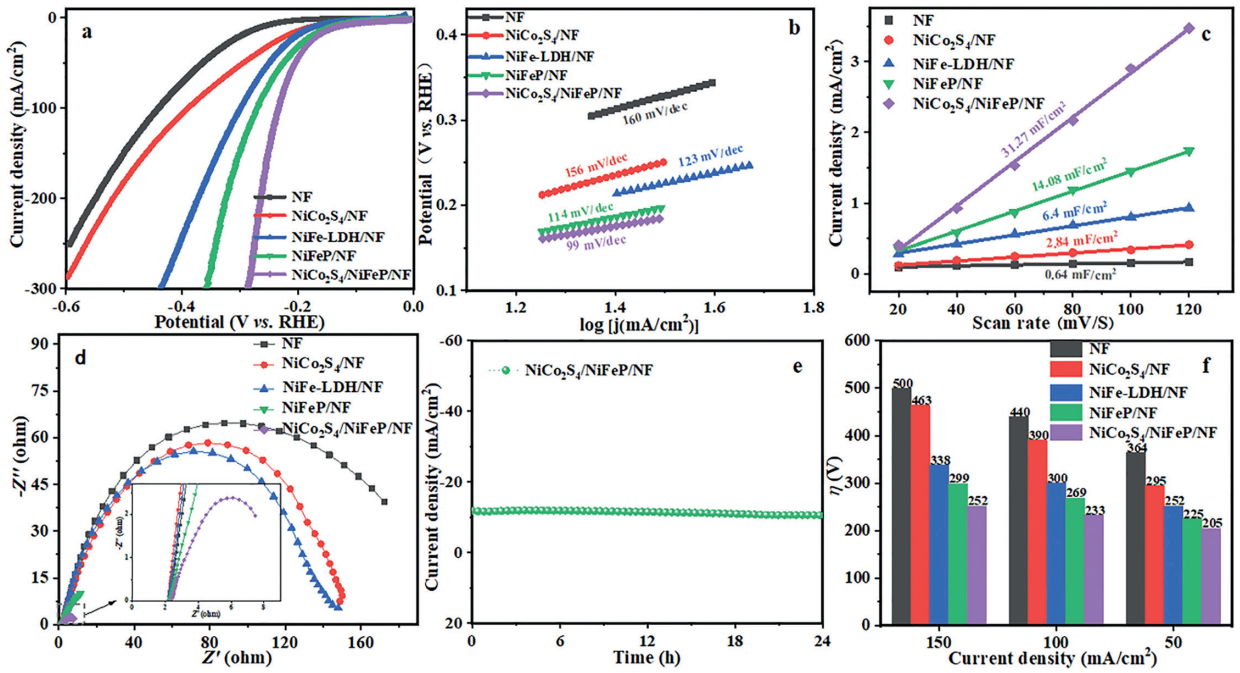

Fig. 5. Electrocatalytic HER performance of $NiCo_2S_4$/NF, NiFe-LDH/NF, NiFeP/NF, $NiCo_2S_4$/NiFeP/NF composite system under 1 mol/L KOH: (a) LSV, (b) Tafel, (c) Cdl, (d) EIS curves and (e) long-term stability test of $NiCo_2S_4$/NiFeP/NF, (f) η required at different current densities.

minimize ohmic loss and effectively promote the integration of electronics and H_{ads} [26,40]. To evaluate the stability of $NiCo_2S_4$/NiFeP/NF, the electrocatalytic activity is measured in 1.0 mol/L KOH with current density of 10 mA/cm^2 for at least 24 h by chronopotentiometry, no significant catalytic performance degradation is observed, indicating high catalytic stability (Fig. 5e). In addition, in Fig. 5f, compared to NF, $NiCo_2S_4$/NF, NiFe-LDH/NF and NiFeP/NF, $NiCo_2S_4$/NiFeP/NF shows excellent hydrogen evolution activity. High electrocatalytic activity and long-term stability establish $NiCo_2S_4$/NiFeP/NF as a promising HER electrocatalyst with potential applications.

Under the same test conditions as HER, the OER performance of $NiCo_2S_4$/NiFeP/NF was further evaluated. Similarly, the optimal NiCo ratio of $NiCo_2S_4$/NiFeP/NF and the electrodeposited ring layer was investigated (Fig. S5 in Supporting information). $NiCo_2S_4$/NiFeP/NF has the best oxygen evolution activity when Ni:Co = 1:1 and the electrodeposited ring layer is 4 circles. For OER, $NiCo_2S_4$/NiFeP/NF requires 293 mV overpotential at current density of 100 mA/cm^2, (Fig. 6a), which is significantly lower than that of pure $NiCo_2S_4$/NF (470 mV) and NiFeP/NF (340 mV). The high OER activity of $NiCo_2S_4$/NiFeP/NF is mainly attributed to the synergistic effect between $NiCo_2S_4$ and NiFeP, as well as the rapid electron transfer and abundant active sites of $NiCo_2S_4$/NiFeP/NF three-dimensional flower-like composite structure. As shown in Fig. 6b, $NiCo_2S_4$/NiFeP/NF has the lowest Tafel slope (110 mV/dec) compared with the $NiCo_2S_4$/NF sample (193 mV/dec) and NiFeP/NF sample (123 mV/dec), which means that it has faster oxygen evolution kinetics. It is conducive to the electro-absorption of OH^- and the generation of OH* [41]. At the same time, the double-layer capacitance (Cdl) value of the electrode was also measured by cyclic voltammetry (CV) at a scan rate of 20–120 mV/s on the sample, and calculated the electrochemical surface area is shown in Fig. 6c. For OER, the double-layer capacitance (Cdl) value of $NiCo_2S_4$/NiFeP/NF is 31.1 mF/cm^2, which is significantly greater than $NiCo_2S_4$/NF (3.34 mF/cm^2), NiFe-LDH/NF (9.2 mF/cm^2) and NiFeP/NF (12.1 mF/cm^2), which is mainly due to the combination of $NiCo_2S_4$ and NiFeP/NF increasing the number of active sites. In addition, compared with $NiCo_2S_4$/NF (R_{ct} = 17.13 Ω) and NiFeP/NF (R_{ct} = 3.52 Ω), $NiCo_2S_4$/NiFeP/NF (R_{ct} = 3.36 Ω) has fast charge transfer capability, as shown in Fig. 6d. Previous work has confirmed that the strong electron interaction between two separate components in the composite electrocatalyst can effectively change the electronic structure, reduce the free energy of the intermediate adsorption orption, and thus improve the catalytic activity [42–45]. In the stability test of 1.0 mol/L KOH, $NiCo_2S_4$/NiFeP/NF could keep stable for at least 24 h at 10 mA/cm^2 without significant degradation of performance (Fig. 6e). In addition, in Fig. 6f, compared to NF, $NiCo_2S_4$/NF, NiFe-LDH/NF and NiFeP/NF, $NiCo_2S_4$/NiFeP/NF shows excellent oxygen evolution activity.

For further check out the origin of OER activity, the $NiCo_2S_4$/NiFeP/NF sample after 24 h stability test was characterized. It is observed that the $NiCo_2S_4$/NiFeP/NF still maintains the three-dimensional nano-spherical structure, however the spherical thickness increased, as shown in Fig. 7a. Among them, the peak at 853.0 eV is attributed to $Ni^{\delta+}$ (δ is close to 0), which may be the exposed Ni matrix after the sulfate falls off [46]. XPS tests illustrate that the metal elements all move towards high binding energy after oxygen evolution (Figs. 7b–d), indicating a tendency to form Ni^{3+}, Fe^{3+}, and Co^{3+} species, promoting M-OOH production, similar phenomenon has also been observed in many previous studies [47–49]. As shown in Fig. S8 (Supporting information), after the OER reaction in the Raman spectrum, NiOOH peaks were observed at both 473 cm^{-1} and 553 cm^{-1} [50], the peak of $NiCo_2S_4$ at 682.5 cm^{-1} becomes weaker [51], and the peak of CoOOH is shown at 824.6 cm^{-1} [52]. Correspondingly, the shift of the binding energy of P element and S element is mainly attributed to the electronic interaction between M (Ni/Fe/Co) [32,33,37,53]. Moreover, $NiCo_2S_4$/NiFeP/NF produces phosphate species [54,55] (Fig. 7e) and sulfate [56,57] (Fig. 7f) after the oxygen evolution reaction. Nevertheless, the relevant literature has also shown that the real active species for oxygen evolution is the corresponding metal hydroxide [54–57]. Therefore, high electrocatalytic activity and long-term stability have established $NiCo_2S_4$/NiFeP/NF as a promising OER electrocatalyst with potential applications.

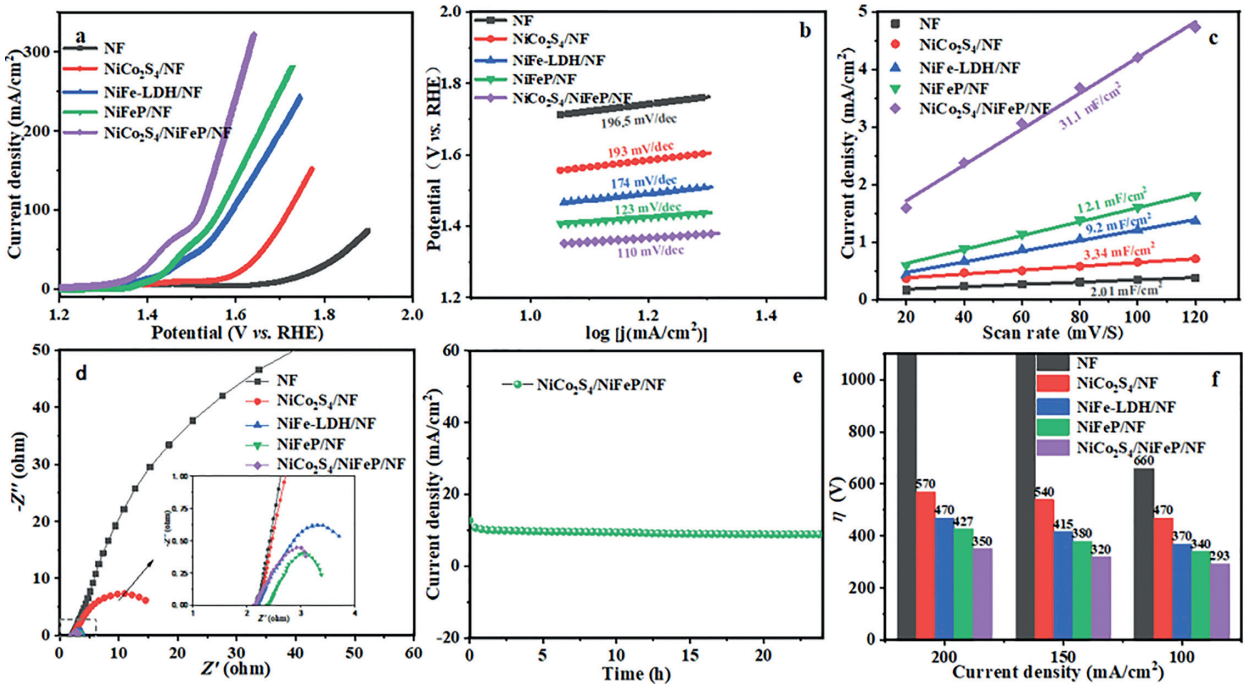

Fig. 6. Electrocatalytic OER performance of $NiCo_2S_4$/NF, NiFe-LDH/NF, NiFeP/NF, $NiCo_2S_4$/NiFeP/NF composite system under 1 mol/L KOH: (a) LSV, (b) Tafel, (c) Cdl, (d) EIS curves and (e) long-term stability test of $NiCo_2S_4$/NiFeP/NF, (f) η required at different current densities.

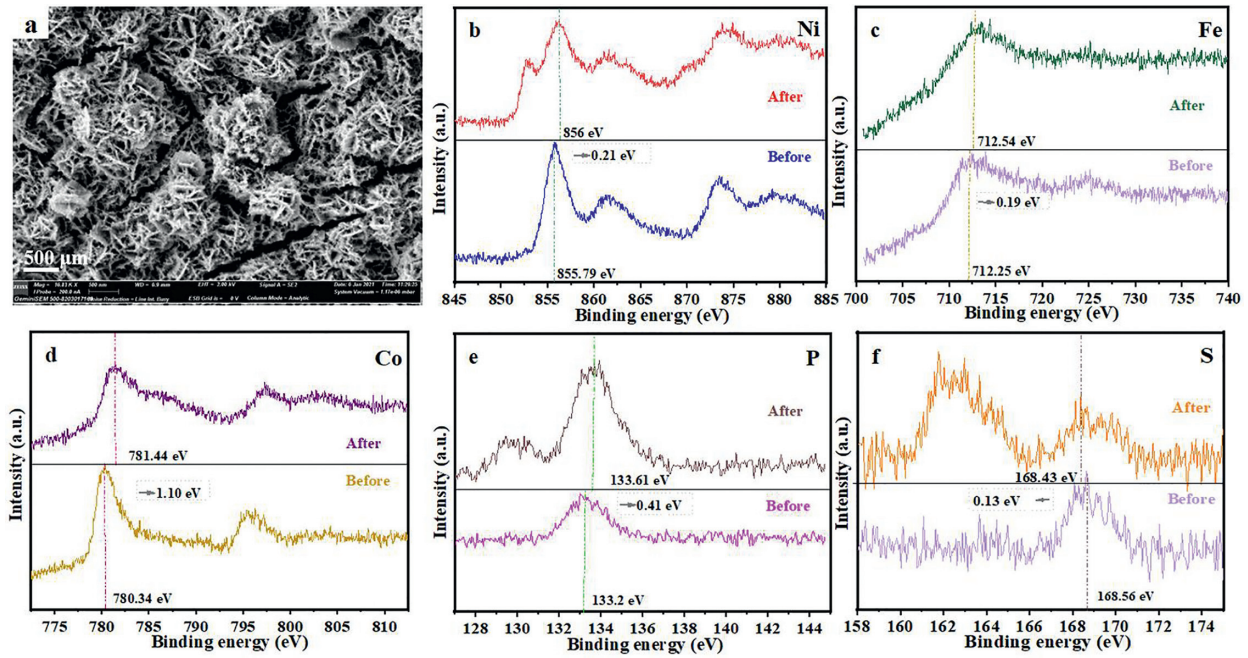

Fig. 7. (a) SEM image of $NiCo_2S_4$/NiFeP/NF after OER stability test. XPS spectra of (b) Ni, (c) Fe, (d) Co, (e) P, (f) S before and after the reaction.

According to the above analysis, it is found that $NiCo_2S_4$/NiFeP/NF has superb hydrogen evolution and oxygen evolution things to do at the same time. $NiCo_2S_4$/NiFeP/NF are used as each cathode and anode to consider the overall water splitting endeavor in 1 mol/L KOH with a two-electrode system. Under the constant voltage current density without IR compensation and the scanning speed of 5 mV/s, the catalytic performance of electrocatalyst in practical application can be more accurately reflected [10]. As shown in Fig. 8a, when $NiCo_2S_4$/NiFeP/NF gives a current density of 10 mA/cm^2, it solely needs a battery voltage of 1.560 V to attain the overall water splitting in 1 mol/L KOH. The general water splitting overall performance of the dual-function electrocatalyst is comparable to the reported composite structure electrocatalyst. For example, $CoMoS_4/Ni_3S_2$ (1.568 V) [58], $NiFe_2O_4$/CoNi–S (1.570 V) [59] and $CoNi_2S_4/Ni_3S_2$ (1.65 V) [60]. Furthermore, the stability of $NiCo_2S_4$/NiFeP/NF was tested, and the current density of 20 mA/cm^2 can be stable operation at 80.2% after 24 h (Fig. 8b). As proven in Fig. S9 (Supporting infor-

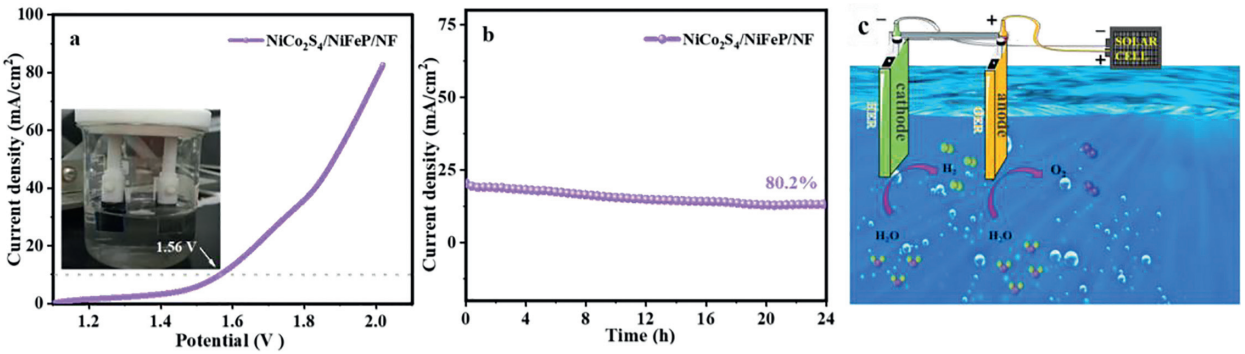

Fig. 8. (a) LSV and (b) stability test curves of $NiCo_2S_4$/NiFeP/NF under 1 mol/L KOH. (c) Illustration of electrocatalytic water splitting over $NiCo_2S_4$/NiFeP.

mation), both the cathode and the anode of the dual-electrode system have bubbles emerging, indicating that the overall water splitting performance of $NiCo_2S_4$/NiFeP/NF is excellent. Finally, using commercially available solar cells (2 V, Tianjin Shixun, 54 mm × 54 mm) for $NiCo_2S_4$/NiFeP/NF||$NiCo_2S_4$/NiFeP/NF cell power supply, and the continuous evolution of H_2 and O_2 bubbles in the two electrodes, confirmed $NiCo_2S_4$/NiFeP/NF composite electric catalyst application value, as shown in (Fig. 8c).

In summary, a three-dimensional flower-like $NiCo_2S_4$/NiFeP/NF electrocatalyst was assembled through a simple one-step hydrothermal method, phosphating and electrodeposition techniques. Furthermore, the reaction mechanism of $NiCo_2S_4$/NiFeP/NF and the reasons for hydrogen evolution and oxygen evolution activity were systematically discussed. Notably, the superb electrocatalytic activity and stability of $NiCo_2S_4$/NiFeP/NF are attributed to the unique three-dimensional flower-like structure, which affords a high specific area and swarming active sites for the reaction. At the same time, the synergistic effect of $NiCo_2S_4$ and NiFeP promotes the rapid transfer of charges, improves the binding energy of the reaction intermediates, and thereby increases the catalytic activity. In the two-electrode system, the high efficiency integral hydrolysis of 10 mA/m^2 is driven at 1.560 V and shows remarkable durability for 24 h. The consequences indicate that the composite is a promising excellent performance bifunctional electrocatalyst. This work gives a high-quality approach for the similar improvement of low-priced and high-efficiency electrocatalysts.

Declaration of competing interest

The authors declare that they have no known competing financial interests or personal relationships that could have appeared to influence the work reported in this paper.

Acknowledgments

This work was financially supported by National Key R&D Program of China (No. 2019YFC1907602) and National Natural Science Foundation of China (Nos. 51572295, 21273285 and 21003157).

Supplementary materials

Supplementary material associated with this article can be found, in the online version, at doi:10.1016/j.cclet.2021.12.028.

References

[1] G.Q. Chen, X.F. Wu, Renew. Sustain. Energy Rev. 69 (2017) 735–749.
[2] K. Christopher, R. Dimitrios, Energy Environ. Sci. 5 (2012) 6640–6651.
[3] F. Guandalini, Campanari, et al., Enrgy Procedia 105 (2017) 1839–1846.
[4] L. Xiao, L. Wang, Petrochem. Ind. Technol. 6 (2016) 98.
[5] T. Zhu, B. Sun, X. Zhu, et al., J. Anal. Appl. Pyrolysis 156 (2021) 105111.
[6] J.E. Brandenburg, U.S. Patent 7037484, 2006.
[7] R.H. Wolk, A.R. Johnson, G. Nongbri, U.S. Patent 3972803, 1976.
[8] R. Shafi, J. Hasselmeyer, A. Bourane, et al., U.S. Patent 9255230, 2016.
[9] H. Dillon, U.S. Patent 10/763712, 2005.
[10] A.S. Joshi, I. Dincer, B.V. Reddy, Int. J. Hydrog. Energy 35 (2010) 4901–4908.
[11] J.Z. Yin, W.B. Wang, C.J. Zhang, et al., Biotechnology 17 (2007) 92–95.
[12] H. Su, S.J. Song, Y.Q. Gao, et al., Adv. Funct. Mater 32 (2022) 2109731.
[13] K. Richa, et al., Renew. Sustain. Energy Rev. 12 (2008) 553–563.
[14] J. Yu, Q. He, G. Yang, et al., ACS Catal. 9 (2019) 9973–10011.
[15] S. Anantharaj, S.R. Ede, K. Sakthikumar, et al., ACS Catal. 6 (2016) 8069–8097.
[16] F. Cheng, Z. Li, L. Wang, et al., Mater. Horiz. 8 (2021) 556–564.
[17] A. Kw, A. Xw, A. Zl, et al., Nano Energy 77 (2020) 105162.
[18] J. Yuan, X. Cheng, C. Lei, et al., Engineering 7 (2021) 1306–1312.
[19] Y. Shi, B. Zhang, Chem. Soc. Rev. 45 (2016) 1529–1541.
[20] X.D. Chen, Z.Y. Pan, C.J. Lei, et al., J. Mater. Chem. A 7 (2019) 965–971.
[21] S. Chandrasekaran, L. Yao, L. Deng, et al., Chem. Soc. Rev. 48 (2019) 4178–4280.
[22] R. Boppella, J. Tan, W. Yang, et al., Adv. Funct. Mater. 29 (2019) 1807976.
[23] A.M. Al-Enizi, A. Nafady, M.M. El-Halwany, et al., Int. J. Hydrog. Energy 44 (2019) 21716–21725.
[24] W. Lin, A. Zl, A. Kw, et al., Nano Energy 7 (2020) 4104850.
[25] F. Cheng, L. Wang, H. Wang, et al., Nano Energy 71 (2020) 104621.
[26] P. Che, Y. Wang, X. Zhang, et al., Ionics 27 (2021) 2139–2150.
[27] H. Su, X. Du, X. Zhang, Int. J. Hydrog. Energy 44 (2019) 30910–30916.
[28] J. Guo, J. Sun, Y. Sun, et al., Mater. Chem. Front. 3 (2019) 842–850.
[29] Z. Niu, C. Qiu, J. Jiang, et al., ACS Sustain. Chem. Eng. 7 (2018) 2335–2342.
[30] D. Zhang, L. Peng, Z. Yang, et al., Inorg. Chem. 58 (2019) 15841–15852.
[31] Y. Shao, Y. Zhao, H. Li, et al., ACS Appl. Mater. Interfaces 8 (2016) 35368.
[32] L. Wan, C. He, D. Chen, et al., Chem. Eng. J. 399 (2020) 125778.
[33] Z.A. Lei, A. Jp, Y.A. Yuan, et al., Appl. Surf. Sci. 557 (2021) 149831.
[34] C. Wu, J. Cai, Y. Zhu, et al., ACS Appl. Mater. Interfaces 9 (2017) 19114–19123.
[35] K. He, T.T. Tsega, X. Liu, et al., Angew. Chem. Int. Ed. 58 (2019) 11903–11909.
[36] R. Ding, M. Zhang, Y. Yao, et al., J. Colloid Interface Sci. 467 (2016) 140–147.
[37] X. Yang, H. Niu, H. Jiang, et al., ChemElectroChem 5 (2018) 1576–1585.
[38] Z. Peng, X. Qiu, G. Cai, et al., J. Alloy. Compd. 842 (2020) 155784.
[39] J.J. Duan, Z. Han, R.L. Zhang, et al., J. Colloid Interface Sci. 588 (2020) 248–256.
[40] B. Mao, P. Sun, Y. Jiang, et al., Angew. Chem. 59 (2020) 15232–15237.
[41] X. Du, J. Huang, D. Yong, Dalton Trans. 46 (2017) 7327–7331.
[42] S. Niu, Y. Sun, G. Sun, et al., ACS Appl. Energy Mater. 2 (2019) 3927–3935.
[43] D. Xiang, X. Bo, X. Gao, et al., J. Power Sources 438 (2019) 226988.
[44] M. Yang, W. Lu, R. Jin, et al., ACS Sustain. Chem. Eng. 7 (2019) 12214–12221.
[45] X. Zhang, L. Zhang, G. Xu, et al., Inorg. Chem. 59 (2020) 12232–12239.
[46] Y. Zhang, J. Fu, H. Zhao, et al., Appl. Catal. B 257 (2019) 117899.
[47] P. Li, C. Du, Z. Zhuang, et al., 2D Mater. 7 (2020) 035016.
[48] Y. Zhang, J. Xu, Y. Ding, et al., Int. J. Hydrog. Energy 45 (2020) 17388–17397.
[49] W. Zhu, W. Chen, H. Yu, et al., Appl. Catal. B 278 (2020) 119326.
[50] J. Zhao, X. Ren, Q. Han, et al., Chem. Commun. 54 (2018) 4987–4990.
[51] Y. Tingting, L. Ruiyi, L. Zaijun, et al., Electrochim. Acta 211 (2016) 59–70.
[52] N. Sanpo, A. Ang, M.F. Hasan, et al., Phases and microstructures of solution precursor plasma sprayed cobalt ferrite splats, in: Proceedings of the Asian Thermal Spray Conference, Tsukuba, Japan, 2012 November 26-28.

[53] X. Huang, H. Xu, D. Cao, et al., Nano Energy 78 (2020) 105253.
[54] D. Chen, Z. Pu, R. Lu, et al., Adv. Energy Mater. 10 (2020) 2000814.
[55] Z. Lei, J. Bai, Y. Li, et al., ACS Appl. Mater. Interfaces 9 (2017) 35837–35846.
[56] L.M. Cao, J.W. Wang, D.C. Zhong, et al., J. Mater. Chem. A 6 (2018) 3224–3230.
[57] M. Khodabakhshi, S. Chen, T. Ye, et al., ACS Appl. Mater. Interface 12 (2020) 36268–36276.
[58] P. Hu, Z. Jia, H. Che, et al., J. Power Sources 416 (2019) 95–103.
[59] Y. Shi, X. Feng, H. Guan, et al., Int. J. Hydrog. Energy 46 (2021) 8557–8566.
[60] W. Dai, K. Ren, Y.A. Zhu, et al., J. Alloy. Compd. 844 (2020) 156252.